



## Regular article

# Characterization of nano-scale oxides in austenitic stainless steel processed by powder bed fusion

Fuyao Yan<sup>a,\*</sup>, Wei Xiong<sup>b,\*\*</sup>, Eric Faierson<sup>c</sup>, Gregory B. Olson<sup>a,d,\*</sup>

<sup>a</sup> Department of Materials Science and Engineering, Northwestern University, Evanston, IL 60201, USA

<sup>b</sup> Department of Mechanical Engineering and Materials Science, University of Pittsburgh, Pittsburgh, PA 15261, USA

<sup>c</sup> Quad City Manufacturing Laboratory-Western Illinois University, Rock Island, IL 61201, USA

<sup>d</sup> QuesTek Innovations LLC, Evanston, IL 60201, USA



## ARTICLE INFO

## Article history:

Received 19 March 2018

Received in revised form 4 June 2018

Accepted 5 June 2018

Available online xxx

## Keywords:

Additive manufacturing

Austenitic stainless steel

Oxide

## ABSTRACT

Nano-scale MnSiO<sub>3</sub> Rhodonite particles were observed in 316L stainless steel fabricated by selective laser melting (SLM). These oxide particles act as Zener-pinning particles providing dragging force to retard grain growth, and enhance strength through the comparison of Hall-Petch effects between SLM 316L and commercial wrought 316L under 1200 °C isothermal heat treatment. The metastable Rhodonite particles were observed to *in-situ* convert to stable MnCr<sub>2</sub>O<sub>4</sub> Spinel particles at 1200 °C, as predicted by computational thermodynamics. This work introduces nano-scale oxides, which are normally detrimental inclusions, as a new type of particle for grain refinement and strengthening through their refinement in additive manufacturing.

Published by Elsevier Ltd on behalf of Acta Materialia Inc.

Additive manufacturing (AM) has received great attention in the past few years for the potential of building complex parts without the design constraints of conventional manufacturing [1]. Selective laser melting (SLM) is a powder bed fusion technique, which utilizes a high-power laser to selectively melt and fuse the pre-laid powders in a layer-by-layer manner. Since the feedstock materials for SLM are in the form of powders, which are manufactured by the inert gas atomization process, there is a much higher likelihood of oxygen contamination in the initial powders. It is reported that the oxygen content in the gas-atomized steel powders is typical ~200 ppm [2]. Due to the low solubility of oxygen in alloys, oxygen typically exists in the form of oxides, whose chemistry is primarily dependent on the oxygen-gettering elements in the alloy. The presence of macro-scale oxide inclusions have been recognized as a major concern in alloys, as they can significantly degrade the mechanical properties, due to the weak metal/inclusion interface or large oxide cracking. Therefore, for conventional manufacturing, the oxygen content is strictly controlled below a certain level (~20 ppm for steel). For AM materials made from powders with high oxygen content, this brings up a concern for the influence of oxide inclusions on the mechanical properties of AM parts. However, few publications have covered the study of oxide inclusions in AM metal builds. Thijs et al. [3] investigated the origin of large irregular-shaped Ti and

Al oxides in SLM maraging steel 18Ni(300) parts. These oxides are sized around 10–100 μm, which are typically detrimental to mechanical properties. On the contrary, nano-scale Si-rich oxide particles were discovered in the laser-melted 316L stainless steel, along with excellent tensile properties in the as-built condition [4–6]. The idea of *in-situ* formation of oxide dispersion strengthening (ODS) steel by AM was therefore proposed [5, 6], but more dedicated studies are still needed to clarify the formation and the impacts of nano-scale oxide inclusions in AM 316L. Since extensive work has been performed to study the deoxidation reactions during solidification in the casting and welding processes [7–10], some knowledge, such as the mechanisms of the formation of oxide inclusions, can be directly applied to the AM process. Additionally, for metallic parts for mission-critical service, mechanical properties are highly demanding. A series of post-process heat treatment is therefore essential before an as-fabricated AM part can transform into an end-user part, and it is also important to investigate the evolution of oxide inclusions during subsequent heat treatment. In this study, 316L stainless steel was built by SLM followed by isothermal heat treatment at 1200 °C. Phase stability and kinetics of oxide particles, along with their impacts on grain structure and mechanical properties were studied.

316L powders (16–44 μm) were produced by Carpenter Powder Products Inc. with the composition listed in Table 1. A 10 mm × 20 mm × 10 mm cube was fabricated by the EOS M270 powder bed fusion system, with 180 W laser power, 1000 mm/s scan speed, 180 μm beam diameter, 0.02 mm layer thickness and 0.09 mm hatch spacing. With the inert gas fusion (IGF) method, the oxygen content in the build was determined to be 0.026 wt%. The as-deposited sample was

\* Corresponding authors at: 2220 Campus Drive, Cook Hall 2036, Evanston, IL 60208, USA.

\*\* Corresponding author.

E-mail addresses: [fuyaoyan2018@u.northwestern.edu](mailto:fuyaoyan2018@u.northwestern.edu) (F. Yan), [weixiong@pitt.edu](mailto:weixiong@pitt.edu) (W. Xiong), [g-olson@northwestern.edu](mailto:g-olson@northwestern.edu) (G.B. Olson).

**Table 1**

Composition (in wt%) of as-built SLM 316L alloy and 316L commercial wrought alloy.

Element	Fe	Cr	Ni	Mo	Mn	Si	Cu	C	S	P	O
Powder	Bal.	16.3	10.3	2.09	1.31	0.49	–	0.026	0.006	0.026	0.040
Commercial alloy	Bal.	16.69	10.09	2.01	1.75	0.41	0.52	0.019	0.0256	0.026	–

cut into 3 mm × 10 mm × 3 mm samples for further heat treatment. Commercial wrought alloy in the form of a cold-rolled square bar (10 mm × 10 mm × 300 mm) was purchased from TA Chen Stainless Pipe Co., LTD. The as-received material (composition in Table 1) was in the rolled and annealed state according to the ASTM A484-13a standard. Pieces of both SLM and the wrought specimens were encapsulated in quartz tubes under vacuum, and then argon back-filled to a pressure of 10<sup>-4</sup> to 10<sup>-2</sup> Torr. Both SLM 316L and commercial wrought samples were heat treated at 1200 °C for 0.5 h, 1 h and 2 h, followed by water quenching. For comparison, one piece of wrought 316L alloy was heat treated at 1200 °C for 12 h to generate a larger grain size. An array of 36 Vickers hardness indentations was performed on all as-polished surfaces by a Clemex MMT microhardness tester, with a load of 100 g and dwell time of 10 s. Revealing grain boundaries was aided by a thin oxide layer, obtained by a high-temperature exposure to air for a couple of seconds. Grain structure analysis was performed by optical metallography and electron microscopy. Grain size was determined by the intercept method based on the ASTM E112-12 standard. SLM 316L samples were further vibratory polished with 0.06 μm colloidal silica for 2 h before the EBSD examination, which was performed in an FEI Quanta ESEM. A thin layer perpendicular to the build direction was taken from the bottom part of the SLM 316L samples in the as-built condition and heat-treated condition. JOEL JEM-2100 FaSTEM and Hitachi HD-2300 Dual EDS Cryo STEM equipped with dual energy-dispersive x-ray spectroscopy (EDX) and electron energy loss spectroscopy (EELS) were used for microstructural analysis on thin foil samples prepared by electropolishing.

Evolution of SLM 316L grain structures during isothermal heat treatment at 1200 °C is illustrated by color-coded orientation imaging microscopy (OIM) in Fig. 1 using electron backscattering diffraction (EBSD). As implied by Fig. 1(a), grains in the as-built condition are mostly columnar along the build direction and are highly textured along <110> directions. The bi-modal distribution of grains and less-textured smaller equiaxed grains shown in Fig. 1(b) indicate the release of residual stress by recrystallization after 30-min heat treatment at 1200 °C. As holding time increases, the smaller equiaxed grains keep growing, consuming textured grains (green area in Fig. 1(b)–(d)), and the number of twins in the FCC structure increases with annealing time. The <110> build direction pole figures for the austenite phase imply that the crystal texture gradually disappears after 30-min annealing. However, grain indexed in green in Fig. 1 still dominate after 2 h, indicating partial recrystallization with most stored energy relieved by recovery.

Thin foils from the bottom layer (x-y plane) of SLM 316L in the as-built condition were observed by scanning transmission electron microscopy in both bright field and Z-contrast mode. As shown in Fig. 2 (a), cellular solidification structures were evident in the bright field mode, with a high density of dislocations at the cell boundaries. In the Z-contrast mode, highly dispersed nano-particles were observed mostly on cell boundaries, as shown in Fig. 2(b). Nano-diffraction on a specific particle allows crystal structure analysis. The diffraction pattern as in Fig. 2(b) includes an FCC structured-pattern for austenite matrix and a set of complex diffraction spots, attributed to the oxides. Line scans across the spherical particles were performed by EDX to estimate

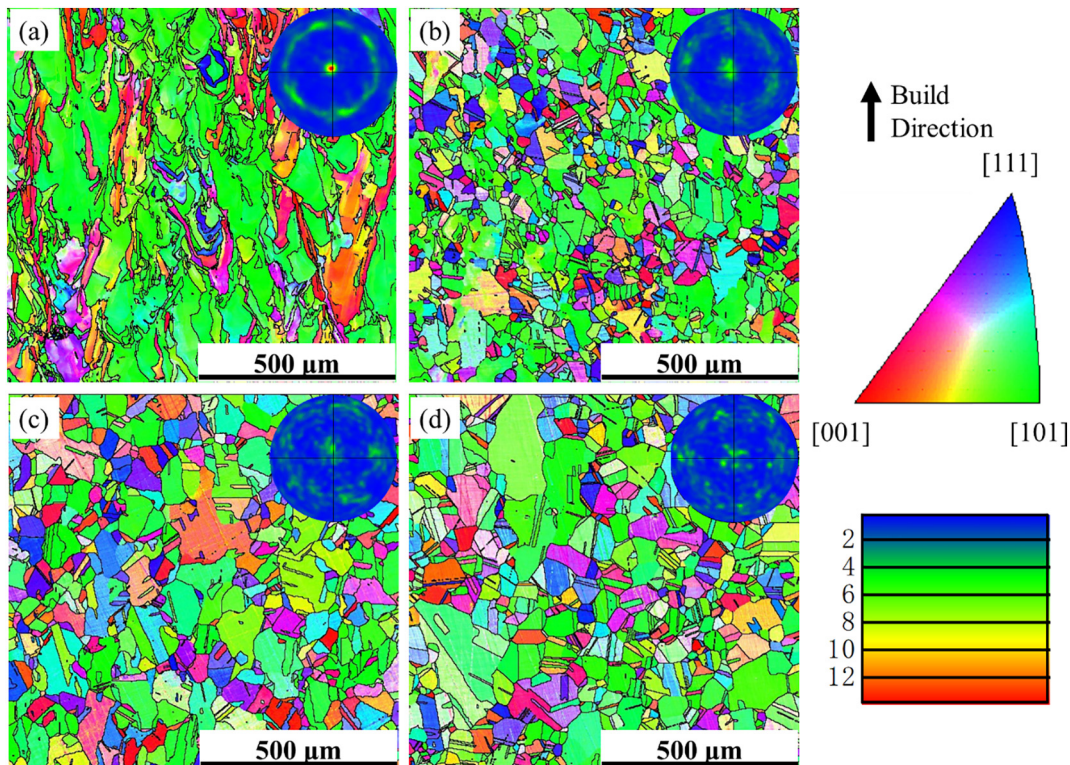


**Fig. 1.** OIM color maps and <110> build direction pole figures for the austenite phase in SLM 316L during isothermal heat treatment at 1200 °C. (a) As-built condition; (b) Heat-treated for 30 min; (c) Heat-treated for 1 h; (d) Heat-treated for 2 h.

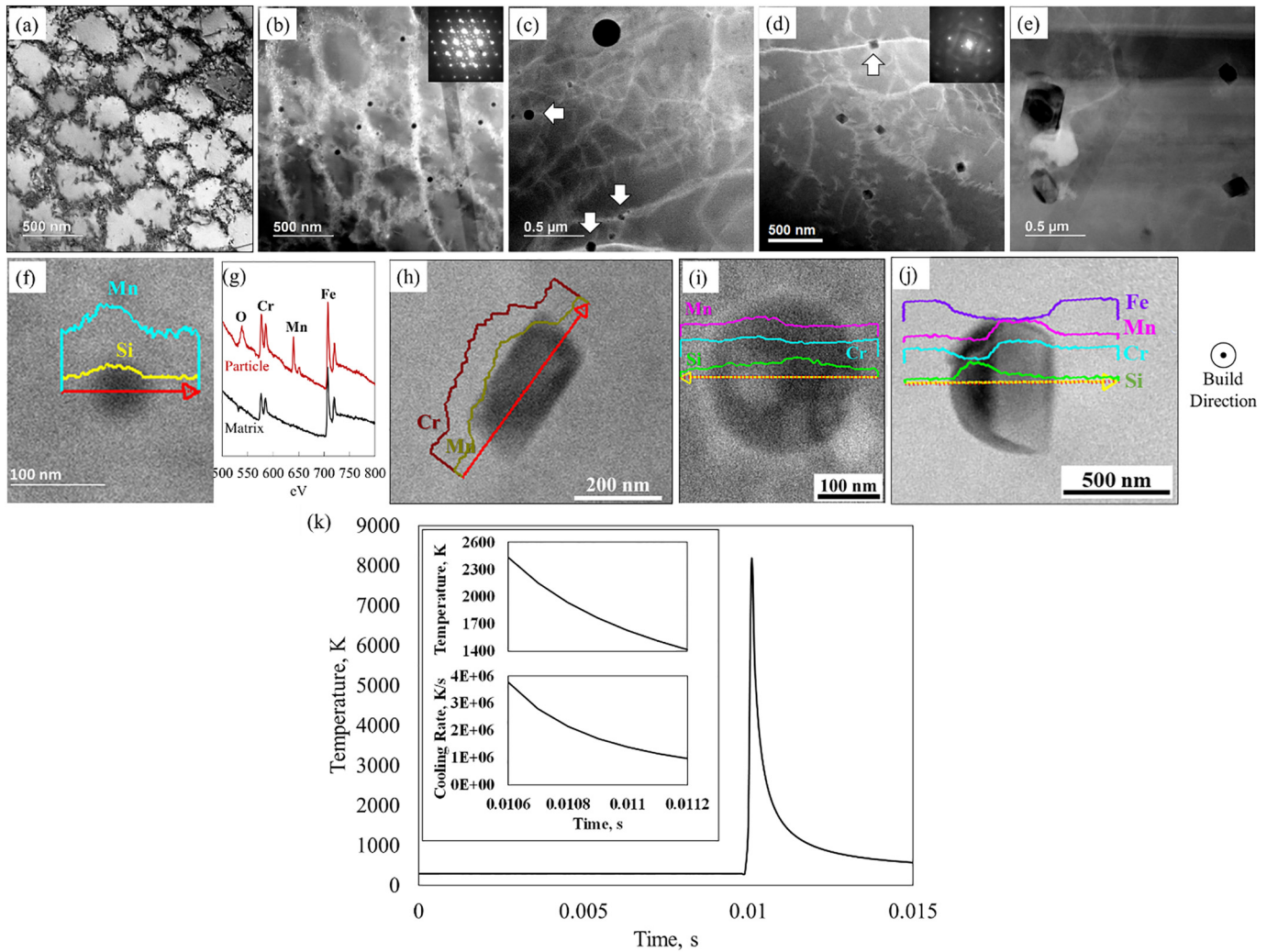


**Fig. 2.** Morphology, composition and crystal structure of oxide particles in the as-built and heat-treated SLM 316L. (a) Cellular structure in the as-built condition (bright field); (b) Spherical particles along cell boundaries in the as-built condition (Z-contrast), with the nano-diffraction pattern for the spherical particles; (c) Spherical particles in the SLM 316L heat treated at 1200 °C for 30 min; (d) Prismatic particles distributed in the SLM 316L heat treated at 1200 °C for 1 h, with the nano-diffraction pattern for the prismatic particles; (e) Prismatic particles in the SLM 316L heat treated at 1200 °C for 2 h; (f) EDX linear scan over a spherical particle in the as-built condition showing the particles rich in Si and Mn; (g) EELS spectrum for particle and matrix in the as-built condition; (h) EDX linear scan over a prismatic particle showing the particles rich in Cr and Mn; (i) EDX linear scan over a large spherical particle with a prismatic particle within in the sample heat treated for 30 min; (j) EDX linear scan over a large spherical particle with a prismatic particle within in the sample heat treated for 1 h; (k) Temperature profile calculated by the Rosenthal approximation. The inset shows the calculated cooling rate within the oxide-formation temperature range.

oxide concentration. It was found that such particles were rich in Mn and Si, as shown in Fig. 2(f). Due to the limitation of EDX on light elements, EELS was adopted to reveal the compositional difference in Si, O, and Mn between the matrix and the particle. Since the energy loss of Si is significantly less than that of O and Mn, a Si peak is not visible in the particle EELS spectrum shown in Fig. 2(h). The chemistry of particles is consistent with  $\text{MnSiO}_3$  Rhodonite, which is typically observed in Mn/Si deoxidized steels [8, 9]. As several thermomechanical simulations have shown that the laser can rapidly heat the melt pool above the boiling temperature ( $\sim 2862$  °C) [11, 12], the initial oxides in the powders can be completely dissolved back into the melt. With the Rosenthal approximation, the temperature-time profile for the single-track scanning can be estimated [13]. Fig. 2(k) shows the calculated temperature history for the spot in the center of the path and 30  $\mu\text{m}$  away from the bottom of the melt pool in the Z-direction, with the processing conditions used for the SLM process. The cooling rate within the oxide-formation temperature range is as high as  $10^6$  K/s. Therefore, during the rapid solidification, the oxide particles can precipitate into fine dispersions. This differs from the large oxide inclusions in cast and weld steel, as initial oxide particles are hardly dissolved and the slow cooling rate promotes the significant growth and coarsening of the

initial oxide particles. [14–16]. After annealing for 30 min, particles are coarsening quickly. However, after annealing for 1 h and longer, almost all spherical particles are replaced by prismatic particles, as shown in Fig. 2(d) & (e). All prismatic particles were found to be rich in Mn and Cr (see Fig. 2(h)). The diffraction pattern identified the particles to be Spinel ( $\text{MnCr}_2\text{O}_4$ ) consistent with JCPDS card (No. 75-1614). A 500 nm spherical particle was captured with a prismatic particle within (see Fig. 2(i)). The prismatic particle is rich in Cr and Mn, and the rest of the spherical particle is rich in Si, indicating the *in-situ* conversion between two types of oxide during the post-process heat treatment. A quantitative analysis of oxide size distribution evolution during

**Table 2**  
Quantitative analysis of oxide size distribution in SLM 316L.

Annealing time (s)	Phase	$r$ (nm)	$N$ ( $1/\text{m}^3$ )
0 (as-built)	Rhodonite	7.09	7.71E21
1800	Rhodonite	32.41	8.04E19
3600	Spinel	24.13	1.62E20
7200	Spinel	98.62	2.37E18

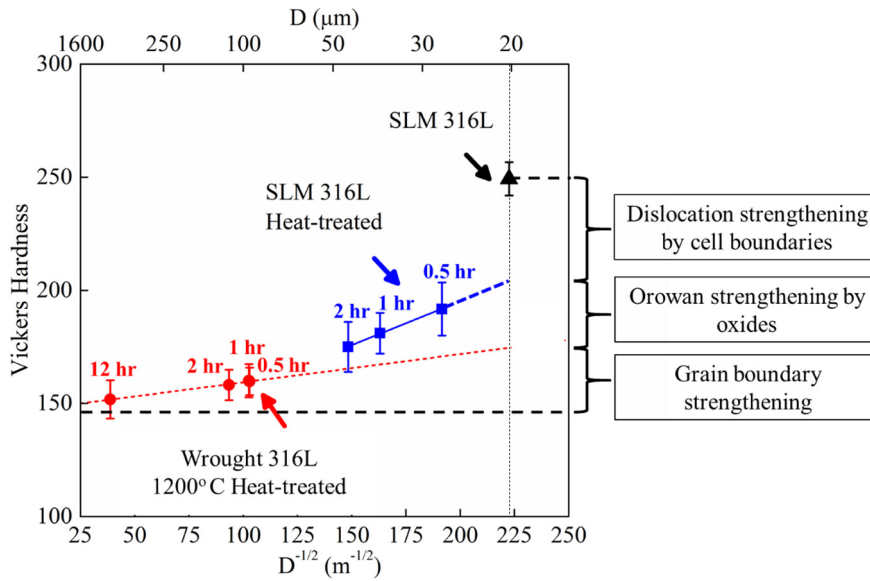


Fig. 3. Relationship of hardness and grain size for SLM 316L in the as-built state (black), SLM 316L in the heat-treated state (blue) and commercial 316L in the heat-treated state (red). (For interpretation of the references to color in this figure legend, the reader is referred to the web version of this article.)

1200 °C heat treatment is listed in Table 2. Since oxide phase transition is observed between 30 min and 1 h, all the oxide particles before 30-min heat treatment are considered as Rhodonite, and all the oxide particles after 1-h heat treatment are treated as Spinel, although in some locations two types of oxides may exist simultaneously. For simplicity, the size of prismatic Spinel particles is taken as the diameter of the equivalent sphere, as the aspect ratio of Spinel particles is  $<2$ . As evident in Fig. 2(c) & (d), both types of oxide particles at grain boundaries can act as pinning particles (pointed by arrows) which retards the motion of grain boundaries.

As indicated in Fig. 3, SLM 316L in the as-built condition exhibits the highest hardness, and the hardness drops with heat treatment. Constructing an effective Hall-Petch relationship among the heat-treated SLM 316L specimens, extrapolation falls short of the hardness in the as-built state. This difference in hardness is primarily attributed to the strengthening effect by high-density dislocations in the form of the cell boundaries, shown in Fig. 2(a). Since the as-built alloy is heat-treated, dislocations recover with a corresponding hardness drop. This

is in accordance with the tensile property comparisons between the as-built and heat-treated AM 316L in previous studies [5, 17]. A true Hall-Petch relationship for grain size strengthening was constructed for the heat-treated commercial rolled and annealed 316L, showing a smaller slope compared with that for the heat-treated SLM 316L. By accounting for the true effect of grain size, the higher hardness in the heat-treated SLM 316L can be attributed to the Orowan strengthening of finely dispersed oxide particles, which decreases as particle coarsens. The intercept of the two lines indicates where the strengthening effect of oxide particles become negligible as particles coarsen with long-time heat treatment.

In order to understand the phase transition of oxide particles observed in isothermal heat treatment at 1200 °C, phase relations were predicted with thermodynamic calculations using the Thermo-Calc software with the TCFE9 Steels thermodynamic database [18]. For the composition of 316L stainless steel, an equilibrium step diagram shown in Fig. 4(a) predicts that the stable phases at 1200 °C are FCC (austenite), Spinel and MnS. The phase transition from Rhodonite to

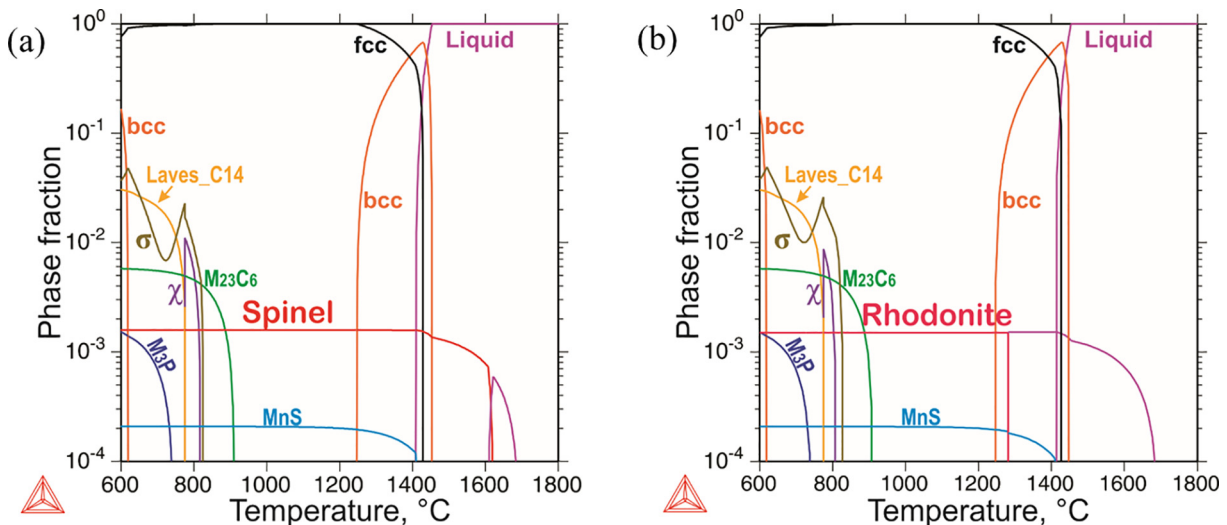


Fig. 4. (a) Equilibrium step diagram for 316L with the composition Fe-16.3Cr-10.3Ni-2.09Mo-1.31Mn-0.49Si-0.026C-0.006S-0.026P-0.026O in wt%. (b) Metastable step diagram with Spinel phase dormant for 316L with the composition Fe-16.3Cr-10.3Ni-2.09Mo-1.31Mn-0.49Si-0.026C-0.006S-0.026P-0.026O in wt%.

Spinel can be explained by calculating the metastable phase diagram as given in Fig. 4(b), where the equilibrium Spinel phase is dormant, and the oxygen-rich Rhodonite phase is predicted with a comparable phase fraction. Since rapid solidification accompanies the AM process, the metastable Rhodonite phase, likely promoted by a lower interfacial energy [13], has a higher rate of nucleation during solidification. During isothermal heat treatment at 1200 °C, Cr gradually diffuses to oxide particles, and Rhodonite is gradually replaced by Spinel, with morphology changing from spherical to prismatic, as evident in Fig. 2(i) & (j).

In summary, this work reveals the ultra-fine oxide inclusions dispersed in the additively manufactured 316L stainless steel. Compared with conventional processing, the high-power laser in AM enables the dissolution of initial oxides in the powders and the rapid solidification of AM refines the dimension of oxide inclusions, turning the normally detrimental oxide inclusions into beneficial nano-scale particles, strengthening the material and retarding grain growth during post-process heat treatment. Such an observation introduces a new type of particle in alloy design with the Zener-pinning effect in addition to conventional pinning particles, such as MC (M = Ti, V, Nb) carbides in steels [19, 20]. This work also investigates the metastability of MnSiO<sub>3</sub> Rhodonite oxides observed in the as-built SLM 316L with the aid of thermodynamic calculations and demonstrates the kinetics of phase transformation from MnSiO<sub>3</sub> Rhodonite phase to the predicted equilibrium MnCr<sub>2</sub>O<sub>4</sub> Spinel phase at 1200 °C. Further studies will apply kinetic simulations of oxide evolution during AM and subsequent heat treatment.

This work was supported by National Institute of Standards and Technology (NIST) through award number 70NANB13H194. Quad City Manufacturing Lab fabricated the materials. The work made use of the MatCI facility and EPIC facility which receive support from the MRSEC Program (NSF DMR-1121262) of the Materials Research Center at

Northwestern University. Microhardness testing was performed in QuesTek Innovations LLC. Wei Xiong is grateful for the support of the Office of Naval Research under contract N00014-17-1-2586.

## References

- [1] D. Herzog, V. Seyda, E. Wycisk, C. Emmelmann, *Acta Mater.* 117 (2016) 371–392.
- [2] E. Klar, P.K. Samal, *Powder Metallurgy Stainless Steels: Processing, Microstructures, and Properties*, ASM International, Materials Park, Ohio, 2007.
- [3] L. Thijs, J. Van Humbeeck, K. Kempen, E. Yasa, J. Kruth, M. Rombouts, *Innov. Dev. Virtual Phys. Prototyp.*, CRC Press, 2011 297–304.
- [4] Y. Morris Wang, T. Voisin, J.T. Mckeown, J. Ye, N.P. Calta, Z. Li, Z. Zeng, Y. Zhang, W. Chen, T.T. Roehling, R.T. Ott, M.K. Santala, P.J. Depond, M.J. Matthews, A.V. Hamza, T. Zhu, *Nat. Mater.* 17 (2018) 63–71.
- [5] Y. Zhong, L. Liu, S. Wikman, D. Cui, Z. Shen, *J. Nucl. Mater.* 470 (2016) 170–178.
- [6] K. Saeidi, L. Kvetková, F. Lofaj, Z. Shen, T. Kaito, T. Narita, S. Jiguang, T. Nishida, M. Fujiwara, *RSC Adv.* 5 (2015) 20747–20750.
- [7] C.S. Chai, T.W. Eagar, *Metall. Trans. B* 12 (1981) 539–547.
- [8] A.O. Klukuken, Ø. Grong, *Metall. Trans. A* 20 (1989) 1335–1349.
- [9] S.S. Babu, S.A. David, J.M. Vitek, K. Mundra, T. DebRoy, *Mater. Sci. Technol.* 11 (1995) 186–199.
- [10] D. You, S.K. Michelic, P. Presoly, J. Liu, C. Bernhard, *Metals* 7 (2017) 460.
- [11] N.E. Hodge, R.M. Ferencz, J.M. Solberg, *Comput. Mech.* 54 (2014) 33–51.
- [12] H.-C. Tran, Y.-L. Lo, *J. Mater. Process. Technol.* 255 (2018) 411–425.
- [13] Ø. Grong, *Metallurgical Modelling of Welding*, 2nd ed. Institute of Materials, London, United Kingdom, 1997.
- [14] B.K. Narayanan, L. Kovarik, P.M. Sarosi, M.A. Quintana, M.J. Mills, *Acta Mater.* 58 (2010) 781–791.
- [15] J.H. Park, *Mater. Sci. Eng. A* 472 (2008) 43–51.
- [16] J.H. Park, *Calphad* 35 (2011) 455–462.
- [17] M. Montero Sistiaga, S. Nardone, C. Hautfenne, J. Van Humbeeck, *Proc. 27th Annu. Int. Solid Free. Fabr. Symp. 2016 - an Addit. Manuf. Conf.*, Austin, TX, United States, 2016 558–565.
- [18] Thermo-Calc Software TCFE9 Steels/Fe-Alloys Database (accessed 5 September 2017).
- [19] G.B. Olson, in: G.B. Olson, M. Azrin, E.S. Wright (Eds.), *Innov. Ultrahigh-strength Steel Technol.*, U.S. Army Laboratory Command, Materials Technology Laboratory, Watertown, Massachusetts 1987, pp. 3–66.
- [20] W. Xiong, G.B. Olson, *npj Comput. Mater.* 2 (2016) 15009.